Neutron spectroscopic studies of the crystal field in $Nd_{2-x-y}Ce_xLa_yCuO_4$ $(0 \leqslant x \leqslant 0.2;\ y = 0.5, 1)$: evidence for a percolative metal-insulator transition

1998 J. Phys.: Condens. Matter 10 7369

(http://iopscience.iop.org/0953-8984/10/33/008)

J. Phys.: Condens. Matter **10** (1998) 7369–7382. Printed in the UK PII: S0953-8984(98)92398-0

Neutron spectroscopic studies of the crystal field in $Nd_{2-x-y}Ce_xLa_yCuO_4$ ($0 \leqslant x \leqslant 0.2$; $y = 0.5$, 1): evidence for a percolative metal–insulator transition

M Gutmann†, P Allenspach†, S Rosenkranz†‡ and A Furrer†

† Laboratory for Neutron Scattering, ETH Zurich and Paul Scherrer Institute, CH-5232 Villigen PSI, Switzerland

‡ Rutherford Appleton Laboratory, Chilton, Didcot, Oxon OX11 0QX, UK

Received 11 March 1998, in final form 26 May 1998

Abstract. Crystal-field (CF) transitions within the ground-state J-multiplet $^4I_{9/2}$ of Nd^{3+} in $Nd_{2-x-y}Ce_xLa_yCuO_4$ ($0 \leqslant x \leqslant 0.2$; $y = 0.5$, 1) have been observed with inelastic neutron scattering. From the CF parameters a negative charge enhancement in the CuO_2 planes is derived upon doping with cerium. Two electronically inequivalent sites in the Ce-doped samples are identified corresponding to undoped and doped micro-regions. Furthermore, the volume fraction of the two components is determined, and it is shown that the metal–insulator transition can be explained by the formation of a two-dimensional percolative network of the doped micro-regions.

1. Introduction

High-temperature superconductors are basically different from classical superconducting compounds in the sense that superconductivity is usually realized through doping, i.e. the homogeneous parent compound is structurally distorted by the doping elements. As a consequence high-temperature superconductors are intrinsically inhomogeneous, and the superconductivity is realized through a percolation process [1]. Such inhomogeneities have actually been observed by a variety of local experimental techniques such as Mössbauer spectroscopy [2], muon spin rotation [3], NMR spectroscopy [4], EXAFS experiments [3], neutron pair distribution studies [5] and most convincingly by neutron crystal-field spectroscopy [6, 7]. The latter technique is based on the fact that in most cuprate superconductors rare-earth ions can be introduced into the system close to the superconducting CuO_2 planes, thus the crystal-field (CF) interaction at the rare-earth site constitutes an ideal probe of the local symmetry as well as the local charge distribution and thereby monitors directly changes of the carrier concentration induced by doping. This has been exemplified for the hole- and electron-doped high-T_c compounds $ErBa_2Cu_3O_{6+x}$ [6] and $Pr_{2-x}Ce_xCuO_{4-\delta}$ [7], respectively, for which selected CF transitions were found to be split into three different components. The spectral weights of these components were found to vary in a continuous and distinct manner with doping, thus they could be associated with local regions of undoped, intermediately doped and highly doped character. A two-dimensional bond percolation model was then able to correctly predict the two-plateau structure of T_c for $ErBa_2Cu_3O_{6+x}$ versus oxygen concentration as well as the critical Ce

0953-8984/98/337369+14$19.50

concentration at the onset of superconductivity in $Pr_{2-x}Ce_xCuO_{4-\delta}$. Raman studies on $R_{1.85}Ce_{0.15}CuO_4$ (R = Pr [8], Nd [9]) revealed similar effects.

In the present work we have studied the compound series $Nd_{2-x-y}Ce_xLa_yCuO_4$ ($0 \leqslant x \leqslant 0.2$; $y = 0.5, 1$) which belong to the class of electron-doped high-T_c compounds with T′ structure. Compared to $Nd_{2-x}Ce_xCuO_4$ the presence of La expands the unit cell volume [10]. Additionally, a wider range for superconductivity is observed. This range extends from $0.14 \leqslant x \leqslant 0.16$ for $Nd_{2-x}Ce_xCuO_4$ to $0.08 \leqslant x \leqslant 0.17$ for $Nd_{1-x}Ce_xLaCuO_4$ after oxygen reduction [10]. For $Nd_{1.5-x}Ce_xLa_{0.5}CuO_4$ the electronic phase diagram has not been determined so far. However, from a linear interpolation the onset of metallic behaviour is expected to occur at $x = 0.11$.

In $Nd_{2-x-y}Ce_xLa_yCuO_4$ the CF potential experienced by the Nd^{3+} ions due to the surrounding ions takes the form

$$V_{CF}(\boldsymbol{r}) = \int_{\boldsymbol{R}} \frac{\rho(\boldsymbol{R})\,\mathrm{d}\boldsymbol{R}}{|\boldsymbol{r} - \boldsymbol{R}|} \tag{1}$$

where $\rho(\boldsymbol{R})$ denotes the electronic charge distribution around the Nd^{3+} ions. The Nd^{3+} ions are very close to the superconducting CuO_2 planes, thus the CF at the Nd^{3+} site constitutes an excellent probe to monitor changes in the local charge distribution or the local structure upon Ce doping. By doping with Ce, electrons are introduced into the compound, since Ce is in the tetravalent state [11], and there is no CF splitting associated with Ce^{4+}.

The present work is organized as follows. In section 2 we describe the sample preparation and the experimental procedure, and in section 3 the observed CF spectra are presented. The CF Hamiltonian is introduced in section 4, and the experimental data are analysed in terms of CF parameters. Significant changes have been observed in the CF parameters as a function of Ce doping, which can be explained by the concept of charge transfer. Moreover, we show that the observed CF spectra correspond to a superposition of two distinctly different CF environments of undoped and doped character. Some final conclusions are given in section 5.

2. Experiment

The samples used in this study were prepared via a sol–gel technique [12]. This technique has proven to produce a better homogeneity in the Ce distribution compared to samples prepared by solid-state reaction [13]. Approximately 20 grams of each compound were prepared. The starting materials were the metal nitrates of Nd, La, Ce and Cu, which were consecutively dissolved in demineralized water in stoichiometric amounts. Then ethylene glycol and citric acid were added to 1.5 times the amount of sample moles. After evaporation of all liquids the resulting gel was heated at a rate of $5\,^{\circ}\mathrm{C\ min^{-1}}$ to $300\,^{\circ}\mathrm{C}$ and left at this temperature for 16 hours. The powder was then heated at the same rate to 500 and $700\,^{\circ}\mathrm{C}$ and left for two hours at each temperature to eliminate all organic by-products. Afterwards the powder was cooled to room temperature at the same rate. The resulting precursor was pelletized and sintered at $1000\,^{\circ}\mathrm{C}$ for 20 hours. Although the samples already appeared as single phase from x-ray diffraction, an additional sintering step at $1000\,^{\circ}\mathrm{C}$ for 100 hours resulted in narrower diffraction peaks indicating an improved sample homogeneity. All samples contained less than 0.9 wt% of CuO which could only be observed by neutron diffraction (figure 1). The samples $NdLaCuO_4$ and $Nd_{0.95}Ce_{0.05}LaCuO_4$ additionally contained about 10% of La_2CuO_4 with T structure. The presence of impurity phases for $x \leqslant 0.1$ was also reported by other groups ([10] and

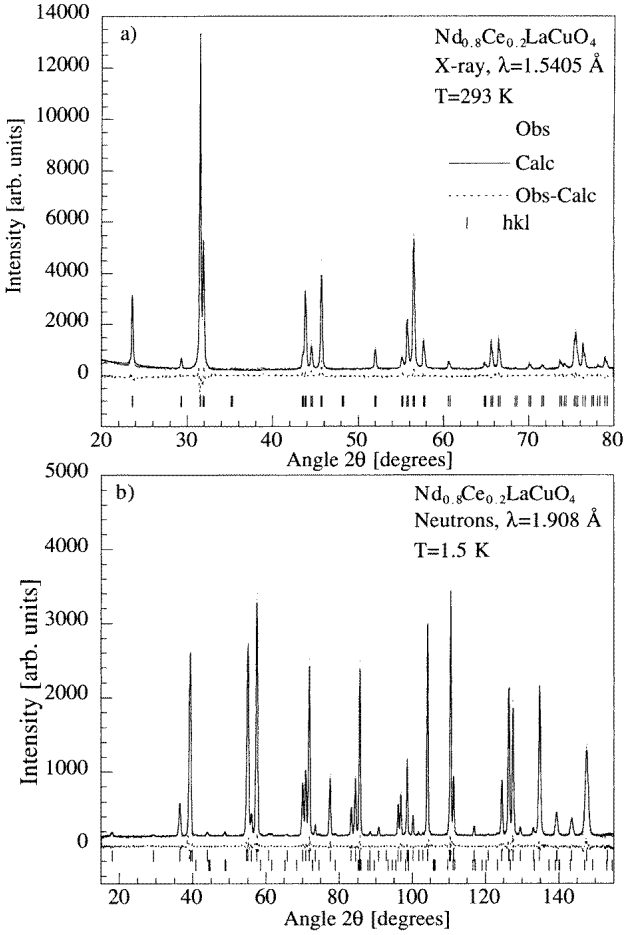

Figure 1. Diffraction patterns of $Nd_{0.8}Ce_{0.2}LaCuO_4$ (a) using x-rays with $\lambda = 1.5405$ Å at room temperature, (b) with neutrons at a wavelength $\lambda = 1.908$ Å at 1.5 K on the powder diffractometer D1A, ILL Grenoble (France). Note that the impurity phase CuO (0.9 wt%, lower *hkl* row) is only seen with neutrons, while the sample appears single phase with x-rays.

references therein). All the samples used in this study were not reduced and are therefore non-superconducting.

Neutron experiments were carried out on the triple-axis spectrometer IN3 at the Institute Laue–Langevin (ILL) in Grenoble (France) and on the direct-geometry time-of-flight spectrometer MARI installed at the spallation neutron source ISIS at the Rutherford Appleton Laboratory (UK). On both instruments the samples were cooled to 10 K using a closed-cycle He refrigerator. A graphite filter was placed after the sample in the case of IN3 to suppress higher order contamination. The scans on IN3 were performed at fixed modulus of the scattering vector and final energy of $Q = 2.7$ Å^{-1} and $E_f = 14.7$ meV, respectively, using the (002) reflection of the pyrolytic graphite analyser. On the monochromator side the Cu(111) reflection was used to access the desired energy transfer range up to 35 meV in the downscattering mode. On MARI the measurements were carried out with a fixed incident energy of 120 meV.

3. Results

3.1. $NdLaCuO_4$ and $Nd_{1.5}La_{0.5}CuO_4$

The CF transitions observed for $NdLaCuO_4$ and $Nd_{1.5}La_{0.5}CuO_4$ are very similar to those reported for La-free Nd_2CuO_4 [14] for which the overall CF splitting is slightly enhanced due to the smaller volume of the unit cell. Characteristic energy spectra obtained for $NdLaCuO_4$ and $Nd_{1.5}La_{0.5}CuO_4$ are shown in figure 2. Four inelastic lines are observed, three of them (A, B, C) in a low-energy window ($15 \leqslant \hbar\omega \leqslant 27$ meV) and one (D) at much higher energy around 90 meV. Their approximate positions are 15, 20.5, 26.6 and 90.5 meV, respectively, thus the CF level scheme in the ground-state J-multiplet $^4I_{9/2}$ is completely determined as illustrated in figure 3(a).

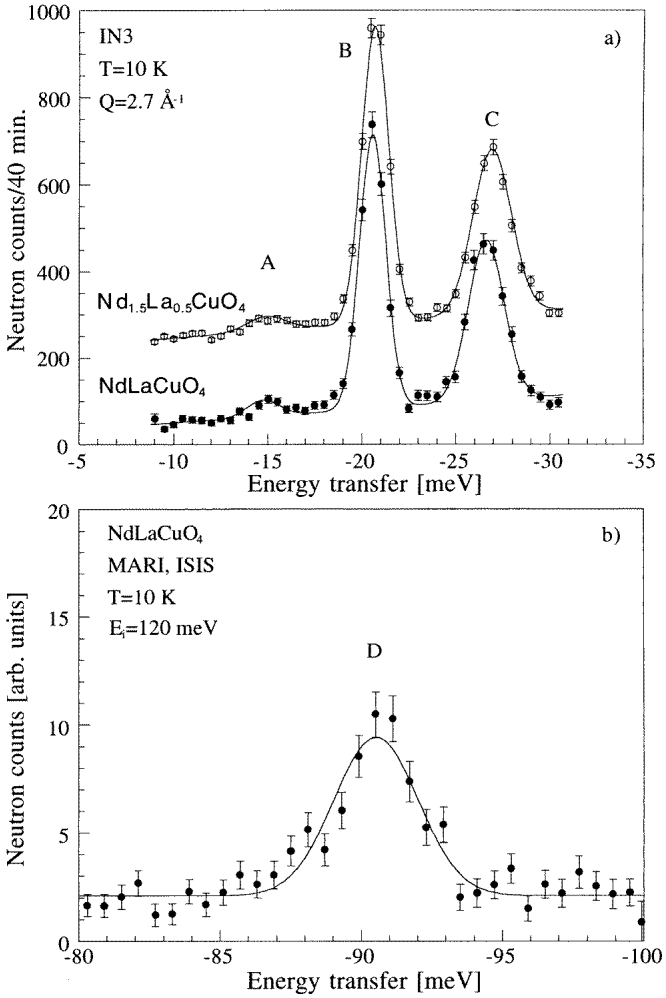

Figure 2. (a) Energy spectra observed for $NdLaCuO_4$ and $Nd_{1.5}La_{0.5}CuO_4$ on IN3. The spectrum of $Nd_{1.5}La_{0.5}CuO_4$ is shifted upwards by 200 counts for the sake of clarity. (b) Energy spectrum observed for $NdLaCuO_4$ on MARI. The lines are least-squares profile fits as explained in the text.

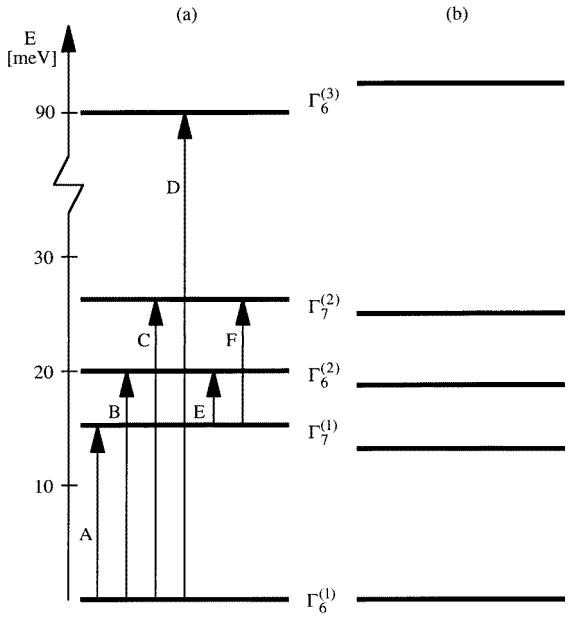

Figure 3. CF level schemes of $Nd_{2-x-y}Ce_xLa_yCuO_4$ ($y = 0.5$, 1) derived for (a) the undoped compound ($x = 0$), (b) the doped micro-regions ($x > 0$). The arrows denote the observed CF transitions.

The magnetic origin of all the inelastic lines can be confirmed by the temperature and Q dependence of the peaks. The partial differential neutron cross section for a CF transition between states $|\Gamma_i\rangle$ and $|\Gamma_j\rangle$ is given in the dipole approximation by [15]

$$\frac{\partial^2\sigma}{\partial\Omega\partial\omega} = \frac{N}{Z}\left(\frac{\gamma e^2}{m_e c^2}\right)^2 \frac{k_i}{k_f}\exp(-2W(\boldsymbol{Q}))F^2(\boldsymbol{Q}) \times \exp\left(-\frac{E_i}{k_B T}\right)|\langle\Gamma_j|J_\perp|\Gamma_i\rangle|^2\delta(E_j - E_i + \hbar\omega). \quad (2)$$

Z is the partition function, $F(\boldsymbol{Q})$ the magnetic form factor, E_i the energy of the ith CF level with wavefunction $|\Gamma_i\rangle$ and $J_\perp$ the component of the total angular momentum operator perpendicular to the scattering vector $\boldsymbol{Q}$. According to (2) the intensity of a CF transition decreases with increasing modulus of the scattering vector according to $F^2(\boldsymbol{Q})$, whereas phonon scattering increases with Q^2 (apart from the modulation due to the structure factor). Furthermore, phonons obey Bose statistics, whereas the population of CF levels is governed by Boltzmann statistics.

The Q and T dependence of the CF transitions is exemplified in figure 4. The Q dependence of the transitions B and C is in agreement with theoretical expectations. The transition A is superimposed on a phononic background [16], so that the expected form factor dependence is not observed. At higher temperatures additional peaks show up at 5 meV and 11.8 meV which can be readily identified as transitions E and F from the first excited to the second and third excited CF states, respectively, thereby confirming the magnetic origin of the transition A. Moreover, the temperature

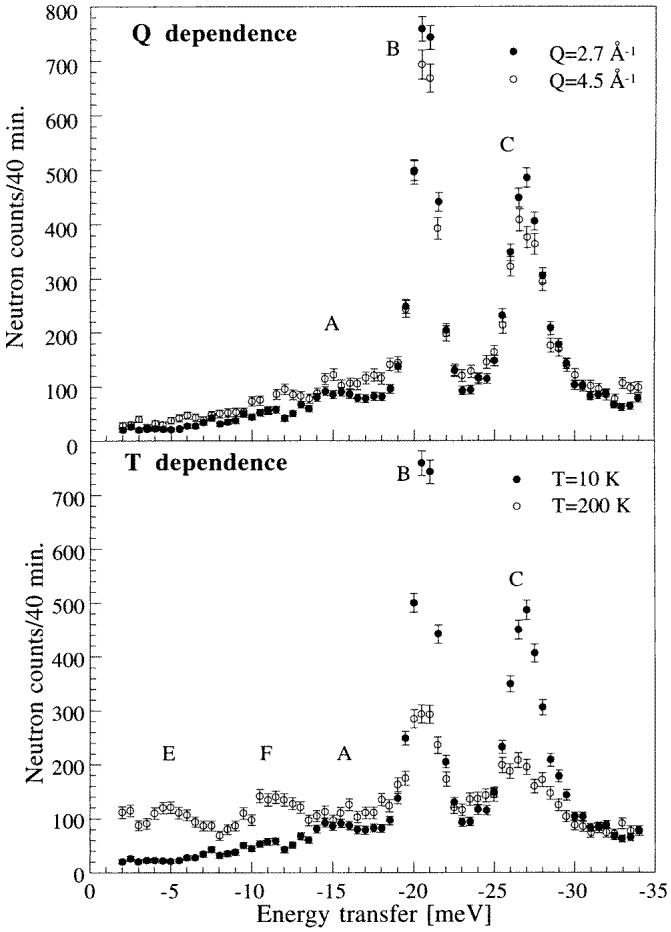

Figure 4. Q and T dependence of the CF excitations observed for $Nd_{1.5}La_{0.5}CuO_4$ on IN3.

dependence of all CF transitions follows quite accurately the Boltzmann population factor.

3.2. Cerium doping effects

Energy spectra are shown in figures 5 and 6. We observe that upon increasing Ce concentration all CF transitions exhibit significant line broadening, which is particularly pronounced for the CF transitions C and D. In addition, the CF transitions in the low energy window are continuously shifted towards lower energies. Compared to the undoped compounds the maximum shifts ($x = 0.20$) are about -2, -0.6 and -0.7 meV for the CF transitions A, B and C, respectively, whereas the CF transition D is slightly shifting upwards. Moreover, the intensitiy of the CF transition A is increasing drastically upon Ce doping.

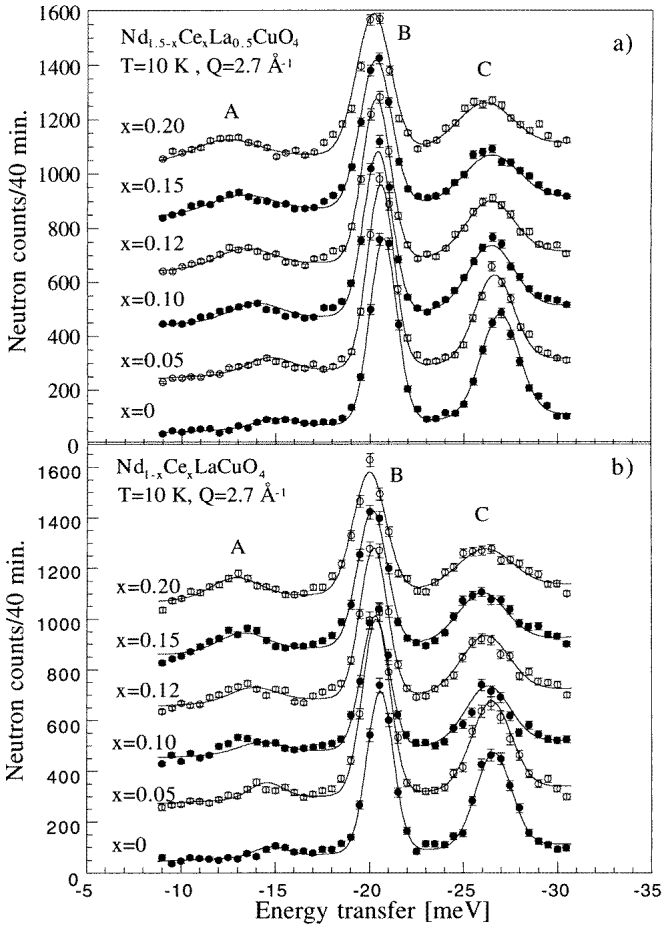

Figure 5. Doping dependence of the CF spectra observed for (a) $Nd_{1.5-x}Ce_xLa_{0.5}CuO_4$ and (b) $Nd_{1-x}Ce_xLaCuO_4$ on IN3. All spectra are consecutively shifted upwards by 200 counts. The lines are least-squares CF profile fits as explained in the text.

4. Analysis of results

4.1. Crystal-field calculation

For the compounds $Nd_{2-x-y}Ce_xLa_yCuO_4$ with tetragonal symmetry the electrostatic potential (1) can be converted into the CF Hamiltonian

$$H_{CF} = A_{20}Y_2^0 + A_{40}Y_4^0 + A_{44}Y_4^4 + A_{60}Y_6^0 + A_{64}Y_6^4 \tag{3}$$

where the A_{mn} denote the CF parameters and the Y_m^n are spherical tensor operators [17]. H_{CF} splits the ground state J-multiplet $^4I_{9/2}$ of Nd^{3+} into five Kramers doublets, and the energies of the excited CF states correspond to the CF splittings A, B, C, D as observed and described in the previous section. Having four energies and two intensity ratios from the experimental data, the five independent CF parameters A_{mn} can directly be determined

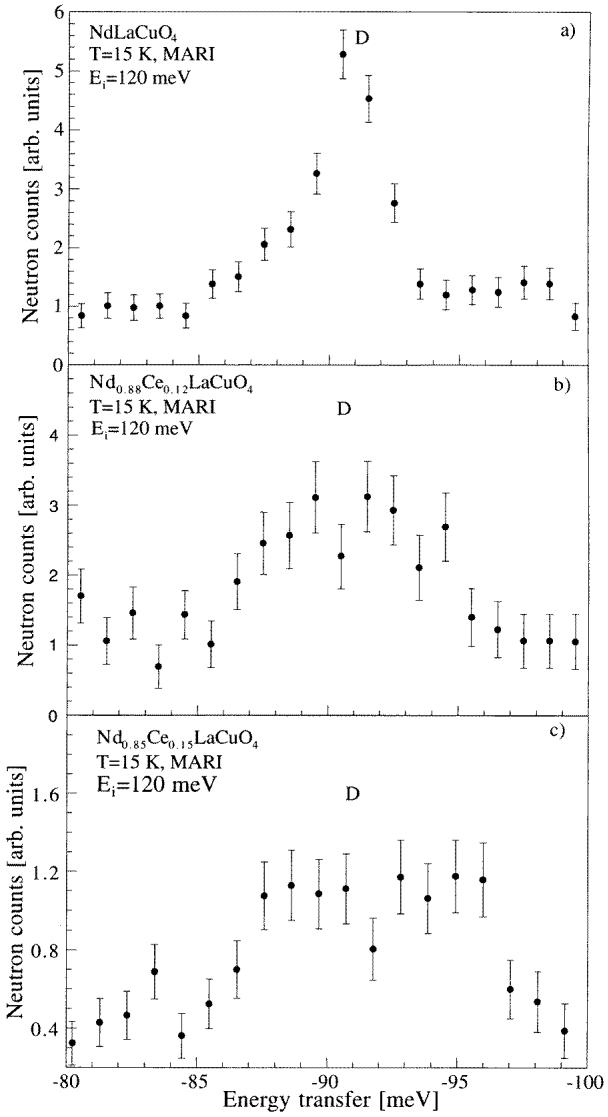

Figure 6. Highest lying CF transition of $Nd_{1-x}Ce_xLaCuO_4$ measured on MARI. The transition exhibits considerable broadening versus Ce doping and is apparently split into two components for $x = 0.15$ (c).

from a least-squares profile fit based on the cross-section formula (2) with Gaussian line-shapes. The inclusion of the first and second excited multiplets with $J = 11/2$ and $13/2$ was found to be important in the CF calculations, since the energy separation between adjacent J-multiplets is of the same order of magnitude as the overall CF splitting, leading to J-mixing effects in the CF ground-state wavefunctions. For details of the J-mixing calculation we refer to [18]. The inclusion of higher lying J-multiplets did not significantly improve the fit. The resulting CF parameters are given in table 1 and figure 7, and the profile fits are visualized in figure 5.

Table 1. CF parameters determined for $Nd_{2-x-y}Ce_xLa_yCuO_4$ ($0 \leqslant x \leqslant 0.2$; $y = 0.5, 1$).

	A_{20} [meV]	A_{40} [meV]	A_{44} [meV]	A_{60} [meV]	A_{64} [meV]
$Nd_{1-x}Ce_xLaCuO_4$					
$x = 0.00$	−5.3(2.8)	−33.2(1.0)	212.9(2.9)	2.19(0.15)	124.8(1.4)
$x = 0.05$	−8.0(2.6)	−35.0(1.4)	215.6(3.3)	1.99(0.19)	123.9(2.2)
$x = 0.10$	−7.4(2.8)	−35.8(1.8)	218.2(4.1)	2.07(0.18)	123.4(2.1)
$x = 0.12$	−9.5(3.1)	−37.1(2.1)	219.2(3.7)	1.98(0.27)	122.7(2.6)
$x = 0.15$	−9.4(3.5)	−38.7(2.2)	222.3(2.7)	1.96(0.30)	120.6(3.4)
$x = 0.2$	−8.4(3.9)	−39.9(1.9)	222.9(1.5)	1.94(0.20)	119.8(3.0)
$Nd_{1.5-x}Ce_xLa_{0.5}CuO_4$					
$x = 0.00$	−5.6(2.4)	−33.8(1.5)	215.5(6.8)	2.19(0.10)	126.5(1.4)
$x = 0.05$	−5.5(2.2)	−35.8(1.9)	223.1(6.6)	2.17(0.19)	124.5(2.4)
$x = 0.10$	−7.8(2.7)	−38.1(2.0)	225.6(4.8)	2.10(0.27)	124.0(4.1)
$x = 0.12$	−7.4(3.1)	−39.6(2.0)	228.3(3.7)	2.14(0.28)	123.3(5.0)
$x = 0.15$	−6.8(3.3)	−40.3(2.2)	229.9(3.4)	2.15(0.24)	122.6(5.1)
$x = 0.20$	−6.6(3.0)	−41.2(2.2)	230.2(2.6)	2.26(0.20)	121.6(4.6)

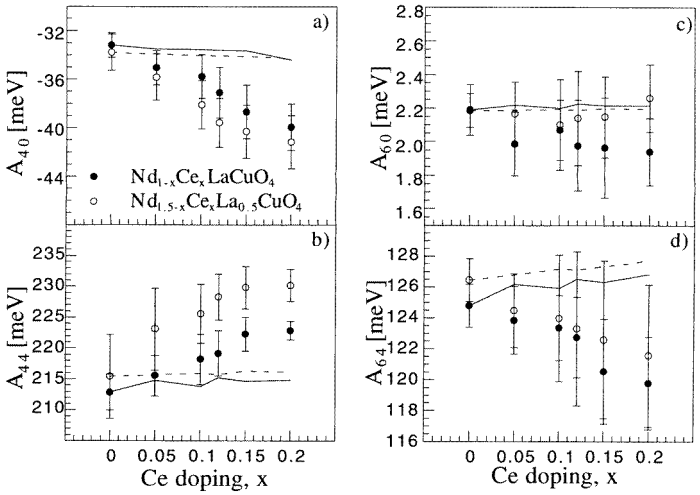

Figure 7. Resulting CF parameters for $Nd_{1.5-x}Ce_xLa_{0.5}CuO_4$ (○) and $Nd_{1-x}Ce_xLaCuO_4$ (●). The dashed and solid lines are the CF parameters expected from structural changes only for $Nd_{1.5-x}Ce_xLa_{0.5}CuO_4$ and $Nd_{1-x}Ce_xLaCuO_4$, respectively.

4.2. Evidence for charge transfer effects

It was shown earlier that some insight into the doping process can be gained by the fact that the rare earths are situated close to the superconducting CuO_2 planes [18]. The presence of additional charge carriers resulting from Ce doping alters locally the electrostatic potential and therefore the CF splitting will be changed. In the framework of the point-charge model the CF parameters can be written in a way to obtain information about the surrounding

charges around the rare-earth ion (see e.g. [19]):

$$A_{nm} = e|e|\langle r^n\rangle \sum_i Z_i \gamma_{nm}(\boldsymbol{r}_i). \tag{4}$$

$\langle r^n\rangle$ denotes the nth moment of the radial wavefunction of the free Nd^{3+} ion, Z_i is the charge of the ith ligand ion situated at $\boldsymbol{r}_i$ with respect to the rare earth, and $\gamma_{mn}(\boldsymbol{r}_i)$ is a geometrical coordination factor [20] that can be calculated from the structural data. Thus the CF parameters are a function of both the structure and the surrounding charges. As shown in earlier work [14, 18] we can restrict our considerations to the nearest neighbour oxygen cuboid with eight oxygen ions at sites O(1) and O(2). Although the point-charge model usually cannot reproduce the observed CF parameters, it was demonstrated that quantitative insight into the doping process can be obtained by considering relative changes of the CF parameters [14, 18]. Assuming structural changes alone we obtain from equation (4):

$$\frac{A_{nm}(x)}{A_{nm}(0)} = \frac{\gamma'_{nm}(x) + \gamma''_{nm}(x)}{\gamma'_{nm}(0) + \gamma''_{nm}(0)}. \tag{5}$$

x denotes the Ce concentration, γ'_{nm} and γ''_{nm} refer to the geometrical coordination factors of the oxygen ions at sites O(1) and O(2), respectively. In figure 7 we compare the experimentally derived CF parameters with the CF parameters obtained from equation (5) from structure changes only. The second order CF parameter is left out due to its long range character. It is evident that structural changes alone cannot explain the experimental CF parameters. This is particularly apparent for the CF parameters A_{40} and A_{44}. However, the presence of additional charge carriers can compensate the differences between the expected and observed CF parameters. From XANES [21] and photoemission experiments [22] it is well known that the additional charge resides in the CuO_2 planes. To quantify the results the additional charge is placed on the four nearest O(1) in the CuO_2 planes, so that equation (4) transforms to

$$A_{nm}(x) = e|e|\langle r^n\rangle Z[[1 + \delta(x)]\gamma'_{nm}(x) + \gamma''_{nm}(x)] \tag{6}$$

where $\delta(x)$ describes the relative charge transfer. Combining (5) and (6) yields:

$$\delta(x) = \frac{A_{nm}(x)}{A_{nm}(0)} \frac{\gamma'_{nm}(0) + \gamma''_{nm}(0)}{\gamma'_{nm}(x)} - \frac{\gamma''_{nm}(x)}{\gamma'_{nm}(x)} - 1. \tag{7}$$

The undoped compound of each series with fixed La content is taken as a reference. The resulting charge transfer $Z\delta(x)$, averaged over the fourth and sixth order CF parameters and assuming $Z = -2$, is displayed in figure 8. The charge transfer corresponds roughly to the number of electrons introduced by Ce doping. This linearity between charge transfer and Ce doping has also been observed in XANES experiments [21]. We note that such an analysis does not take into account local strains or inhomogeneities. Both effects lead to broadened CF transitions affecting mainly the line-width, which is clearly observed. The CF analysis however is based on peak positions and intensities.

4.3. Inhomogeneous treatment: separation into undoped and doped micro-regions

As outlined in section 4.2 the main changes in the CF spectra upon increasing the Ce content can be explained by the presence of electrons doped into the CuO_2 planes. However, effects such as the splitting of the highest lying CF transition D into two peaks as well as the broadening of the CF transitions versus Ce doping cannot be understood in this simple picture. One explanation for these observations could be a line broadening of the CF transitions due to magnetic correlations between Nd^{3+} ions. However, this effect should

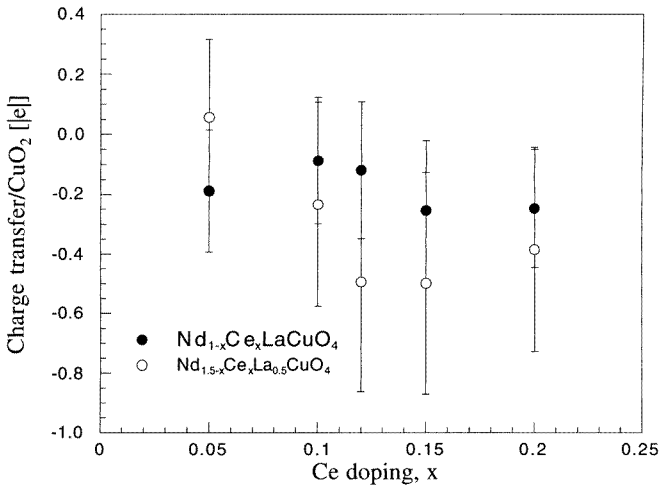

Figure 8. Resulting charge transfer per CuO_2 unit versus Ce doping for $Nd_{1.5-x}Ce_xLa_{0.5}CuO_4$ (○) and $Nd_{1-x}Ce_xLaCuO_4$ (●) calculated from the weighted average over the fourth and sixth order CF parameters.

be most pronounced in the low doping regime, in contrast to our observations. Moreover, such correlations have been found to lead to an overall dispersion of the CF energy levels of the order of 1 meV [23], which is smaller than our instrumental energy resolution and therefore cannot influence the observed spectra. Following the interpretation from earlier inelastic neutron scattering and Raman work on related compounds [7, 9], we will make use of the CF interaction as a local probe and thereby interpret the observed energy spectra as a superposition of two distinctly different CF spectra corresponding to undoped and doped micro-regions. The decomposition is visualized for $Nd_{1-x}Ce_xLaCuO_4$ in figure 9 and was performed as described below.

For a fixed La content ($y = 0.5$, 1) all the energy spectra available for different Ce doping were fitted simultaneously, and a common slope for the background was used. Each CF transition in the low energy window was treated as a superposition of two Gaussian components with equal line widths corresponding to undoped and doped micro-regions, see figures 3(a) and (b), respectively. For the undoped micro-regions the energies and relative intensities of the CF transitions were essentially fixed at the values observed for the undoped compound ($x = 0$). For the doped micro-regions, on the other hand, the energies of the CF transitions were treated as adjustable parameters, and the intensities were correlated to each other according to the calculated transition matrix elements which turned out to be considerably different from those for the undoped micro-regions. For both La concentrations ($y = 0.5$, 1) the CF interaction of the doped micro-regions was found to be identical within the experimental error. A further fitting parameter was the intensity ratio of the CF response for both undoped and doped micro-regions which was found to decrease monotonically with increasing Ce doping. For the series of spectra with $y = 1$ the fitting errors χ^2 are 2.33 and 2.65 for the two-phase and one-phase model, respectively. Similarly, for the $y = 0.5$ series we obtain $\chi^2 = 2.18$ and 2.74, thus justifying our approach. The volume fractions of both micro-regions can then readily be derived by correcting the resulting intensity ratio with the corresponding transition matrix elements. The resulting volume fractions are displayed in figure 10. We realize that the number of doped micro-regions rises continuously with

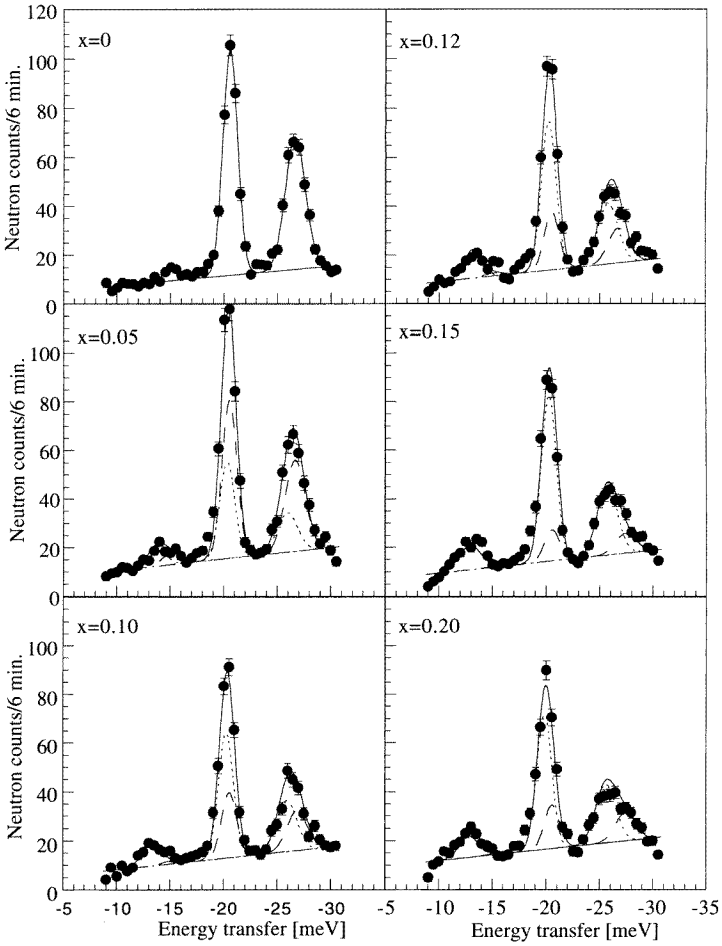

Figure 9. Decomposition of the energy spectra observed for $Nd_{1-x}Ce_xLaCuO_4$ into two components. The dashed and dotted lines correspond to the response of the undoped and doped micro-regions, respectively.

increasing Ce doping as expected. The critical volume fraction of 50% for two-dimensional bond percolation [24] is reached at $x \approx 0.10$ and $x \approx 0.07$ for $Nd_{1.5-x}Ce_xLa_{0.5}CuO_4$ and $Nd_{1-x}Ce_xLaCuO_4$, respectively, which is in excellent agreement with the observed onset of macroscopic metallic behaviour [10]. Therefore it can be concluded that the metal–insulator transition has a percolative character. Similar results were obtained for hole-doped $ErBa_2Cu_3O_{6+x}$ [6] and electron-doped $Pr_{2-x}Ce_xCuO_{4-\delta}$ [7].

5. Conclusion

We have presented an analysis of inelastic neutron scattering experiments of the CF interaction of Nd^{3+} in $Nd_{1.5-x}Ce_xLa_{0.5}CuO_4$ and $Nd_{1-x}Ce_xLaCuO_4$ for the doping range $0 \leqslant x \leqslant 0.2$. The systematic variation of the CF parameters with increasing Ce doping is shown to result from a charge transfer of electrons to the CuO_2 planes which was quantitatively established. Besides this integral picture we have performed an analysis

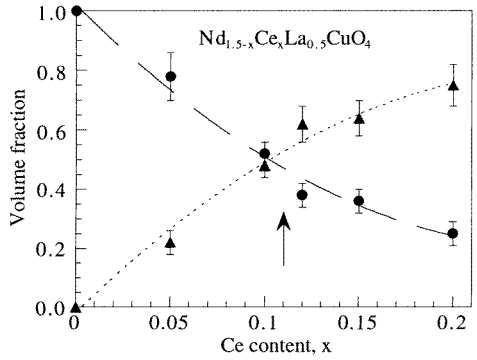

(*a*)

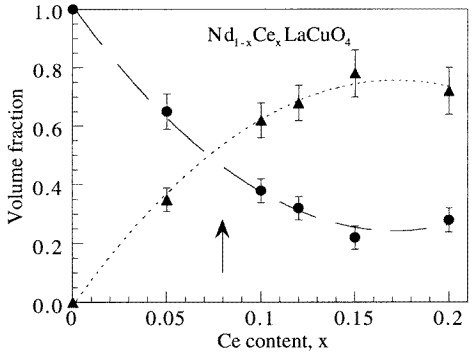

(*b*)

Figure 10. Volume fractions of the undoped (triangles) and doped (circles) micro-regions for (a) $Nd_{1.5-x}Ce_xLa_{0.5}CuO_4$ and (b) $Nd_{1-x}Ce_xLaCuO_4$. The arrow indicates the metal–insulator transition [10]. The lines are guides to the eye.

in which the CF response is treated as a superposition of two components corresponding to undoped and doped micro-regions. The relative volume fractions of undoped and doped micro-regions were determined, and it is found that the metal–insulator transition occurs when the volume fractions of the doped micro-regions reach a critical limit of 50%, which means that the superconductivity in $Nd_{2-x-y}Ce_xLa_yCuO_4$ results from the formation of a two-dimensional percolative network of doped micro-regions.

Acknowledgments

Financial support by the Swiss National Science Foundation is gratefully acknowledged. We are grateful to R S Eccleston, F Fauth and M Zolliker for their assistance in the experimental work.

References

[1] Hizhnyakov V and Sigmund E 1988 *Physica* C **154** 655
[2] Hodges J A, Bonville P, Imbert P, Jéhanno G and Debray P 1991 *Physica* C **184** 270
[3] Sigmund E and Müller K A (eds) 1994 *Phase Separation in Cuprate Superconductors* (Berlin: Springer)

[4] Bakharev O, Dooglav A, Esorov A, Krjukov E, Sakhratov Y, Teplov M, Brom H and Witteveen J 1996 *JETP Lett.* **64** 398
[5] Billinge S J L and Egami T 1993 *Phys. Rev.* B **47** 14 386
[6] Mesot J, Allenspach P, Staub U, Furrer A and Mutka H 1993 *Phys. Rev. Lett.* **70** 865
[7] Henggeler W, Cuntze G, Mesot J, Klauda M, Saemann-Ischenko G and Furrer A 1995 *Europhys. Lett.* **29** 233
[8] Sanjurjo J A, Martins G B, Pagliuso P G, Granado E, Torriani I, Rettori C, Oseroff S and Fisk Z 1995 *Phys. Rev.* B **51** 1185
[9] Jandl S, Dufour P, Strach T, Ruf T, Cardona M, Nekvasil V, Chen C, Wanklyn B M and Piñol 1996 *Phys. Rev.* B **53** 8632
[10] Zhu Y T and Manthiram A 1993 *Phys. Rev.* B **49** 6293
[11] Tokura Y, Takagi H and Uchida S 1989 *Nature* **337** 345
[12] Jardim R F, Ben-Dor L and Maple M B 1993 *J. Alloys and Compounds* **199** 105
[13] Serquis A, Prado F and Caneiro A 1995 *Physica* C **253** 339
[14] Furrer A, Allenspach P, Mesot J and Staub U 1990 *Physica* C **168** 609
[15] Trammell G 1953 *Phys. Rev.* **92** 1387
[16] Sumarlin I, Lynn J, Neumann D, Rush J, Loong C-K, Peng J and Li Z 1993 *Phys. Rev.* B **48** 473
[17] Judd B R 1963 *Operator Techniques in Atomic Spectroscopy* (New York: McGraw-Hill)
[18] Mesot J, Allenspach P, Staub U, Furrer A, Mutka H, Osborn R and Taylor A 1993 *Phys. Rev.* B **47** 6027
[19] Mesot J and Furrer A 1997 *J. Supercond.* **10** 623
[20] Hutchings M T 1964 *Solid State Physics* vol 16, ed F Seitz and D Turnbull (New York: Academic) p 227
[21] Liang G, Guo Y, Badresingh D, Xu W, Tang Y, Croft M, Chen J, Sahiner A, Beam-Hoan O and Markert J T 1995 *Phys. Rev.* B **51** 1258
[22] Klauda M, Ströbel J P, Schlötterer J, Grassmann A, Markl J and Saemann-Ischenko G 1991 *Physica* C **173** 109
[23] Henggeler W, Chattopadhyay T, Rössli B, Vorderwisch P, Thalmeier P, Zhigunov D I, Barilo S N and Furrer A 1997 *Phys. Rev.* B **55** 1269
[24] Kirkpatrick S 1973 *Rev. Mod. Phys.* **45** 574